

Properties of Two Dimensional Transition Metal Silicates

Kayahan Saritas,¹ Nassar Doudin,² Eric Altman,² and Sohrab Ismail-Beigi¹

¹*Department of Applied Physics, Yale University, New Haven, CT, 06520*

²*Department of Chemistry, Yale University, New Haven, CT, 06520*

Two-dimensional van der Waals (2D vdW) single layered materials with ferromagnetism and piezoelectricity have been the subject of recent attention. Despite numerous studies on 2D ferromagnetic materials, developing an air stable and transferable vdW material that is multiferroic has been challenging. To address this problem, we studied layered transition metal silicates that are derivatives of kaolinites and lizardites with transition metals substituting on Al^{3+} and Mg^{2+} sites using *ab initio* Density Functional Theory (DFT) calculations. This class of materials are appealing because they meet the symmetry requirements for piezoelectricity, can host a range of transition metal cations, and as oxides are inherently stable in air. Following our previous experimental work, we predict that these compounds are stable under varying O_2 partial pressure and can be synthesized using a surface assisted method. We also show that the oxidation states of the substituted transition metal ions can be tuned through the level of hydrogenation and possibly by mixing of the transition metal atoms.

I. INTRODUCTION

Two-dimensional van der Waals (2D VDW) materials that display ferromagnetism, piezoelectricity, and ferroelectricity have received increased attention [1–4]. VDW stacking of multiple 2D layers with these complementary properties can help develop multifunctional materials such as multiferroics [5–7]. Despite the fact that there are various well-studied piezoelectric 2D materials available [8, 9], developing an air-stable and transferable VDW single layered material whose ferromagnetism can be tuned under electric or elastic field has been challenging. Air stability is an important problem in this regard as it presents significant challenges in isolating and studying the single layers [10]. Single layers of CrI_3 [10], $\alpha\text{-In}_2\text{Se}_3$ [11] and CuInP_2S_6 [12, 13] were recently isolated experimentally and reported to be ferromagnetic. $\text{Cr}_2\text{Ge}_2\text{Te}_6$ [14] and FePS_3 [15] are also shown to be ferromagnetic, but similarly they suffer from sensitivity to oxidation. In comparison, the search space for ferroic oxide VDW layers remains under-explored. Oxides have the advantage of being stable under ambient conditions, e.g., most metals spontaneously form a thin layer of metal oxide on their surfaces [16].

Transition metal silicate sheets, which have been grown on metal substrates via annealing at elevated temperatures [17–19], are air stable. Thanks to the open-shell transition metal atoms, their magnetic properties can also be tailored. Growing a 2D transition metal silicate starts with depositing SiO and the transition metal ion, such as Ti [19], Fe [17] and Ni [18], at modest temperatures, which then followed by annealing above 950 K. In all these cases the transition metal silicate thermodynamically competes with the formation of bilayer SiO_2 [20–24]. However, parameters such as annealing time, temperature, oxygen pressure, Si and transition metal coverage can facilitate metastable phase formation. As 2D Ti-silicate [19] can be grown on metal substrates, using these experimental methods it should be possible to synthesize first row transition metal silicates films with

smaller transition metal ions (considering the relatively large size of the Ti atom) with a judicious choice of substrate. The resulting transition metal silicates resemble crystal structures of naturally existing sheet silicates (phyllosilicates), particularly that of dehydroxylated nontronite, $\text{M}_2\text{Si}_2\text{O}_8$ [17, 25] as in Fig. 1a. The competing bilayer SiO_2 would be composed of a six-membered ring of SiO_4 tetrahedra with out-of-plane mirror symmetry. In the nontronite case, however, the transition metal polyhedra still form six-membered rings, but they are rotated in such a way so that all the polyhedra are five-fold coordinated. In nontronite, therefore, the ring of metal polyhedra has four edge-sharing and two corner-sharing connections.

Even though nontronite-like 2D transition metal silicates are synthesized on metal substrates, it is possible that closely related crystals, such as kaolinite [26] and lizardite [27] which are also phyllosilicates, can also coexist under similar thermodynamic conditions. Kaolinite and Lizardite have the chemical formulae $\text{Al}_2\text{Si}_2\text{O}_9\text{H}_4$ and $\text{Mg}_3\text{Si}_2\text{O}_9\text{H}_4$, hence their dehydroxylated forms are $\text{Al}_2\text{Si}_2\text{O}_9$ and $\text{Mg}_3\text{Si}_2\text{O}_9$, as shown in Fig. 1b-c. It is known that transition metal atoms such as Fe , Ni , and Co can almost fully substitute Al and Mg in these crystals and similar phyllosilicates [28–33]. Greenalite ($(\text{Fe}^{2+}, \text{Fe}^{3+})_{2-3}\text{Si}_2\text{O}_9\text{H}_4$) [34] and nepouite/pecoraite ($\text{Ni}_3\text{Si}_2\text{O}_9\text{H}_4$) [35, 36] crystals correspond to the Fe - and Ni -substituted kaolinite and lizardite. Magnetic properties of greenalite were previously studied and *intrasheet* ferromagnetic order was observed [37]. It was argued that 90° Fe^{2+} -O- Fe^{2+} interactions lead to net magnetisation in the 2D layer [37]. Therefore, there is a large chemical space to be explored that could be engineered for 2D ferromagnetism. Additionally, the crystalline space groups of kaolinite and lizardite break inversion symmetry, thus these compounds are automatically piezo-active [38].

In this work, we used density functional theory with Hubbard- U correction (DFT+ U) to study structural, energetic, magnetic, electronic and piezoelectric properties of 2D transition metal silicates. We have stud-

ied the derivatives of nontronite $M_2Si_2O_8H_x$, kaolinite $M_2Si_2O_9H_x$ and lizardite $M_3Si_2O_9H_x$ as isolated 2D layers in vacuum at various degrees of hydrogenation, where $M=Cr, Mn, Fe, Co, Ni$ and $x=0-4$. Each transition metal derivative is investigated systematically. For each compound, we report oxidation states of the transition metals, formation and hull energies, energy differences between antiferromagnetic and ferromagnetic phases and average magnetic moments. Additional data describe the stability regions for compounds that are on the convex hull as well as Gibbs free energies of hydrogenation. Finally, piezoelectric properties are reported for the thermodynamically stable and some metastable layers.

II. METHODS

All DFT calculations were performed using the Vienna ab initio Simulation Package (VASP) [39, 40], using the Perdew-Burke-Ernzerhof (PBE) [41] exchange-correlation functional along with the Hubbard- U approach (PBE+ U) [42]. We employ U values of 3.7 eV for Cr, 3.9 eV for Mn, 5.3 eV for Fe, 3.32 eV for Co and 6.2 eV for Ni for all transition metal oxides using the guidelines in Materials Genome Project [43, 44]. These U values were determined according to their accuracy in reproducing the formation energies of all known binary metal oxides [43]. Elemental compounds, whose energies are needed for constructing phase diagrams, are calculated using PBE. PBE and PBE+ U energies are combined using an established mixing scheme calibrated using binary oxide formation energies [43]: the PBE and PBE+ U mixing scheme provides compositional correction parameters for each atom. Similar composition-based corrections are widely used to correct DFT energies to construct phase diagrams [45, 46].

To construct the phase diagrams, we use a procedure based on prior work by Persson *et al.* [47]. To determine the chemical potentials of any compound i under standard conditions, μ_i^0 , we define reference chemical potentials, μ_{ref}^0 , such that $\mu_i^0 = g_i^0 - \mu_{ref}^0$, where g_i^0 is the Gibbs free energy of the species i under standard conditions. Gibbs free energy is defined as $g_i^0 = h_i^0 - Ts_i^0$, where h and s are enthalpy and entropy respectively. Thus, if the reference is at standard conditions, we can simplify as $\mu_i^0 = h_i^0 - h_{ref}^0$ and here, $h_{ref}^0 = E_i^{0,DFT}$, where $E_i^{0,DFT}$ the DFT ground-state energy for the elemental solid. Phase diagrams in this work are constructed using elemental solids, solid oxides, oxygen, hydrogen and water, which are then used to calculate relative stabilities of transition metal silicates. Due to the difficulties in treating such a broad range of materials accurately with a single choice of DFT functional, we resort to several practical approximations and empirical corrections to obtain μ_i^{ref} for each compound. For elemental solids, we approximate as $\mu_i^{ref} \approx E_i^{0,DFT}$ () hence $s_i(T) = 0$. For oxygen gas, however, the reference chemical poten-

tial is defined as $\mu_O^{ref} = E_O^{0,DFT} + \Delta E_O^{corr} - Ts_O^{ref}$ where ΔE_O^{corr} is the oxygen gas correction term added to DFT calculations to better reproduce experimental binary oxide formation energies [48]. The reference, *ref*, here depends on the pressure/temperature of the gases. We use the entropy s_O^{ref} from prior work Kubaschewski *et al.* [49]. For a binary solid oxide, A_xO_y , like the elemental solids, we approximate the entropic terms as negligible [47] and write the chemical potential for that compound as $\mu_{A_xO_y}^0 = E_{A_xO_y}^{DFT} - x\mu_A^{ref} - y\mu_O^{ref}$. Water is a particularly difficult case for most theoretical methods. Therefore, we use the free energy of formation of H_2O at room temperature, $\mu_{H_2O}^0 = -2.46$ eV/ H_2O . The hydrogen chemical potential depends on the chemical potential of H_2O and O, hence it is obtained indirectly as follows. Using the water formation reaction, we define $\mu_H^{ref} = 1/2[g_{H_2O}^{ref} - \mu_O^{ref} - \mu_{H_2O}^0]$. Here, $g_{H_2O}^{ref} = E_{H_2O}^{0,DFT} - Ts_{H_2O}^0$. Numerical values for the variables discussed here are provided in the Supplementary Information along with a more detailed explanation and examples.

We calculate elastic tensor coefficients, C_{ij} , with no ionic relaxations, using the finite differences method and the strain coefficients of the piezoelectric tensor, e_{ij} , via the Berry phase method [50, 51] in VASP. An orthogonal supercell was used to calculate the elastic and piezoelectric constants. A gamma-centered reciprocal space grid of $4 \times 8 \times 1$ (corresponding to a grid density of 120 \AA^{-3}) for sampling the first Brillouin zone and an energy cutoff of 520 eV are used in all our calculations. We ensured a spacing of minimum 30 Å of vacuum between the periodic images of layers in all calculations. Dipole corrections [52] were also included along the out-of-plane direction to reduce spurious interactions between periodic images.

III. RESULTS AND DISCUSSION

Using the phase diagram generation procedure described in the Methods section, we study the stabilities of all the transition metal silicates (from Cr to Ni) shown in Fig. 1 and 2 at varying hydrogenation levels. We consider three structural templates for these transition metal silicates. These templates are based on natural minerals or are ones that have been synthesized. These are nontronite-like silicates $M_2Si_2O_8H_n$ where $n = 0 - 2$, kaolinite-like silicates $M_2Si_2O_9H_n$ where $n = 0 - 4$, and lizardite-like silicates $M_3Si_2O_9H_n$ where $n = 0 - 4$. In Fig. 2, these structures are shown with the highest degree of hydroxylation possible. Kaolinite has two additional oxygens compared to nontronite, and all transition metal polyhedra in kaolinite are six-fold coordinated and edge-sharing. Lizardite, on the other hand, has one additional metal atom compared to kaolinite, which makes the metal oxide layer triangular, as opposed to the honeycomb lattice in kaolinite. Once the structural stabilities are explained (section III A, we describe other computed

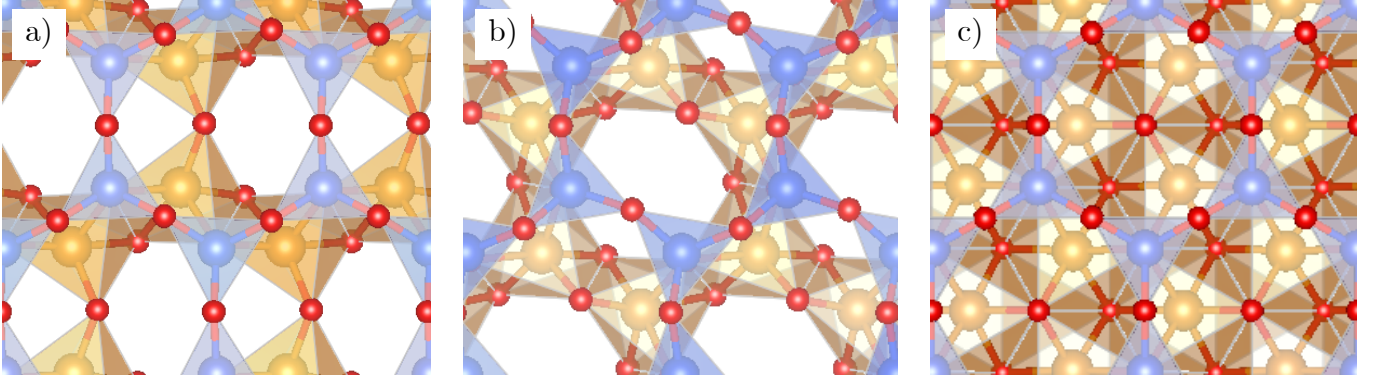


FIG. 1. Top view of the structural templates of the isolated 2D silicate layers studied in this work: a) nontronite-like, b) kaolinite-like, and c) lizardite-like transition metal silicates. Blue, red and orange indicate Si, O and transition metal atom sites, respectively. Blue polyhedra highlight Si-O polyhedra, and gold polyhedra surround the transition metals.

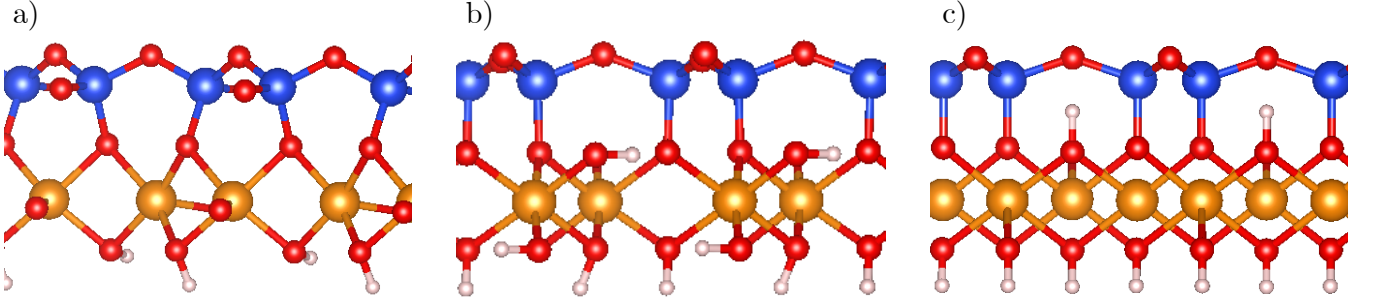


FIG. 2. Side view of the 2D isolated (a) nontronite-like, (b) kaolinite-like, and (c) lizardite-like hydrogenated transition metal silicates. All possible sites for hydrogen binding are shown with hydrogen atoms in white. As per Fig. 1, blue, red and orange indicate Si, O and transition metal atom sites, respectively.

physical properties (remaining sections).

A. Thermodynamic Stabilities

1. Fe-silicates

In Table I, we show the average oxidation number, transition metal electronic configuration, formation and hull energies and average Fe magnetic moments for all the Fe-silicates studied. Average oxidation numbers, N_{ox} , are determined by assuming O and Si to be closed shell ions (i.e., O^{2-} and Si^{4+} ions). The N_{ox} can be used with the transition metal electronic configuration (EC) to show that a charge ordered structure is found. EC is determined by using the magnetic moment on the transition metal atoms and also chemical intuition. For example, for $Fe_3Si_2O_9$ with $N_{ox} = 3.33+$ and EC of d^4, d^5 indicates that one of the Fe atoms is d^4 (4+) and the other two are d^5 (3+). We find that this structure is monoclinic (Cm , #8) with $\gamma=119.64^\circ$. However, when the same structure is forced to have trigonal symmetry ($P31m$, #157), the energy is increased by 0.05 eV/f.u., and all three Fe atoms become magnetically identical (as

expected when constrained to be magnetically collinear). Similar symmetry breaking and charge disproportionation is observed in all structures with non-integer N_{ox} in Table I.

The convex hull energies, E_{hull} , in Table I are determined using a Fe-Si-O-H quaternary phase diagram [53]. The only compounds that have zero hull energy in Table I are $Fe_2Si_2O_9H_4$ and $Fe_3Si_2O_9H_4$. Although Fe-nontronites were shown to exist [17] on Ru (111) substrate, Table I shows that this phase is unstable in isolation even when it is fully hydrogenated. Nevertheless, in all the compounds, there is a clear trend of decreasing hull energy with hydroxylation. However, it is possible that metastable compounds (e.g., $E_{hull} < 50$ meV/atom) can be kinetically trapped making them experimentally accessible. In the literature, a tolerance on the DFT hull energies of around 10 meV/atom is used to eliminate false negatives on the convex hull [54]. However, the smallest non-zero hull energy in Table I is 23 meV/atom, which is well above this likely tolerance of DFT error.

In Fig. 3, we show the chemical stability ranges for $Fe_3Si_2O_9H_4$ as a function of the O and Fe chemical potentials, μ_O and μ_{Fe} . We assume that our quaternary compound (here $Fe_3Si_2O_9H_4$) is in equilibrium with the

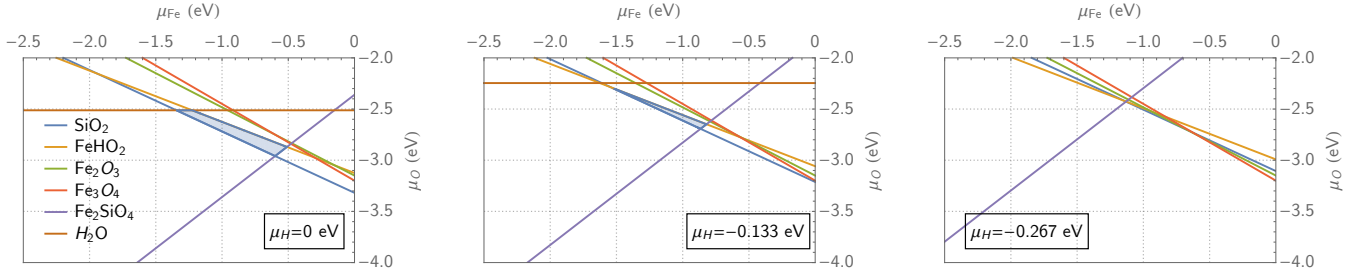


FIG. 3. Phase diagrams for 2D $\text{Fe}_3\text{Si}_2\text{O}_9\text{H}_4$ with a) hydrogen chemical potential μ_H is set to 0 eV, b) $\mu_H = -0.133$ eV and c) $\mu_H = -0.267$ eV. Stability regions of $\text{Fe}_3\text{Si}_2\text{O}_9\text{H}_4$ are shaded in blue.

TABLE I. Average oxidation number of the Fe atoms (N_{ox}^{Fe}), Fe electronic configuration (EC), calculated formation enthalpies (E_f in eV/atom) and energy above the convex hull (E_{hull} in eV/atom) for the 2D iron silicates studied in this work. Average magnetic moment per Fe atom (μ_M in μ_B /atom) in the high-spin FM state is provided. Compositions on the hull of the phase diagram are in bold font.

Material	N_{ox}^{Fe}	EC	E_f	E_{hull}	μ_M
<i>Nontronites</i>					
$\text{Fe}_2\text{Si}_2\text{O}_8$	4+	d^4	-2.253	0.175	2.19
$\text{Fe}_2\text{Si}_2\text{O}_8\text{H}$	3.5+	d^4, d^5	-2.236	0.122	2.56
$\text{Fe}_2\text{Si}_2\text{O}_8\text{H}_2$	3+	d^5	-2.220	0.078	2.96
<i>Kaolinites</i>					
$\text{Fe}_2\text{Si}_2\text{O}_9$	5+	d^3	-2.023	0.218	3.53
$\text{Fe}_2\text{Si}_2\text{O}_9\text{H}$	4.5+	d^3, d^4	-2.027	0.163	3.82
$\text{Fe}_2\text{Si}_2\text{O}_9\text{H}_2$	4+	d^4	-2.039	0.106	3.87
$\text{Fe}_2\text{Si}_2\text{O}_9\text{H}_3$	3.5+	d^4, d^5	-2.037	0.054	4.08
$\text{Fe}_3\text{Si}_2\text{O}_9\text{H}_4$	3+	d^5	-2.042	0.000	4.35
<i>Lizardites</i>					
$\text{Fe}_3\text{Si}_2\text{O}_9$	3.33+	d^4, d^5	-2.327	0.091	4.10
$\text{Fe}_3\text{Si}_2\text{O}_9\text{H}$	3+	d^5	-2.292	0.066	4.30
$\text{Fe}_3\text{Si}_2\text{O}_9\text{H}_2$	2.67+	d^5, d^6	-2.184	0.050	4.03
$\text{Fe}_3\text{Si}_2\text{O}_9\text{H}_3$	2.34+	d^5, d^6	-2.095	0.023	3.93
$\text{Fe}_3\text{Si}_2\text{O}_9\text{H}_4$	2+	d^6	-2.015	0.000	3.75

reservoirs, so that there are three independent chemical potentials. We choose μ_{Fe} and μ_O as the two of the independent parameters for our study and fix the third, μ_H , at various values to understand how the stability regions are modified. Three different μ_H values are selected based on the maximum, average and minimum μ_H where $\text{Fe}_3\text{Si}_2\text{O}_9\text{H}_4$ can exist based on the calculated phase diagram. In general, a "facet" of phase diagram using convex hull formalism indicates a hull member, or in other words it means an $N-1$ dimensional geometric domain on the convex hull where a set of compounds that can coexist in equilibrium. Here, N is the number of compounds used to construct the phase diagram. In a binary convex hull phase diagram, for example, there are two compounds, hence the dimension of a facet would be

one. In this case the facet has a special name called tie-line and each tie-line connects two points on the phase diagram which coexist on this tie-line. For a quaternary compound, a facet is then a three dimensional object which is formed by connecting four points in the convex hull phase diagram. These four points correspond to four compounds that coexist within the three dimensional convex hull facet. All the facets of the quaternary phase diagram where $\text{Fe}_3\text{Si}_2\text{O}_9\text{H}_4$ is found to be thermodynamically stable are given in the Supplementary Information (SI) [53]. For example, $\mu_H=0$ eV is possible on a facet, where $\text{Fe}_3\text{Si}_2\text{O}_9\text{H}_4$ - H_2 - SiO_2 - H_2O can coexist. However, $\mu_H=-0.267$ eV is obtained from the $\text{Fe}_3\text{Si}_2\text{O}_9\text{H}_4$ - Fe_2SiO_4 - FeHO_2 - SiO_2 facet. Therefore, the stability of $\text{Fe}_3\text{Si}_2\text{O}_9\text{H}_4$ is bounded by $0 > \mu_H > -0.267$ eV, but the stability regions of $\text{Fe}_3\text{Si}_2\text{O}_9\text{H}_4$ in Fig. 3 are bounded with the SiO_2 , FeHO_2 , Fe_2SiO_4 and H_2O curves in total. With μ_H is fixed, the H_2O coexistence curves in Fig. 3 are always horizontal. In Fig. 4, we perform the same analysis on $\text{Fe}_3\text{Si}_2\text{O}_9\text{H}_4$ and find that the stability region, where no other phase precipitates, is very small in all cases compared to Fig. 3.

There are various trends that can guide experimental synthesis. Decreasing the hydrogen chemical potential yields a smaller stability region, hence hydrogen rich environments should more easily yield $\text{Fe}_3\text{Si}_2\text{O}_9\text{H}_4$. Next, we find that the stability region of $\text{Fe}_3\text{Si}_2\text{O}_9\text{H}_4$ is mainly controlled by competition with SiO_2 and FeHO_2 . In addition, phase separation into binary oxides is not relevant in the presence of hydrogen. Next, under fixed μ_O , increasing the μ_{Fe} , will lead to precipitation of FeHO_2 , and decreasing μ_{Fe} (increasing μ_{Si}) will lead to precipitation of SiO_2 . Under fixed μ_{Fe} , increasing μ_O (decreasing μ_{Si}) will generally lead to formation of FeHO_2 . In Fig. 3a, there is a small region near $\mu_{Fe} < -1.3$ eV, where increased μ_O will first lead to precipitation of H_2O and then FeHO_2 will follow.

We compare the stability curves of $\text{Fe}_2\text{Si}_2\text{O}_9\text{H}_4$ in Fig. 4 to the stability curves of $\text{Fe}_3\text{Si}_2\text{O}_9\text{H}_4$ in Fig. 3. Our main finding is that the stability region is much smaller compared to Fig. 3. In Fig. 4a, for example, it is a very small region around $\mu_{Fe}=-1.5$ eV and $\mu_O=-2.3$ eV. We believe the relatively small size of the stable region in both figures is primarily due to the fact that both the

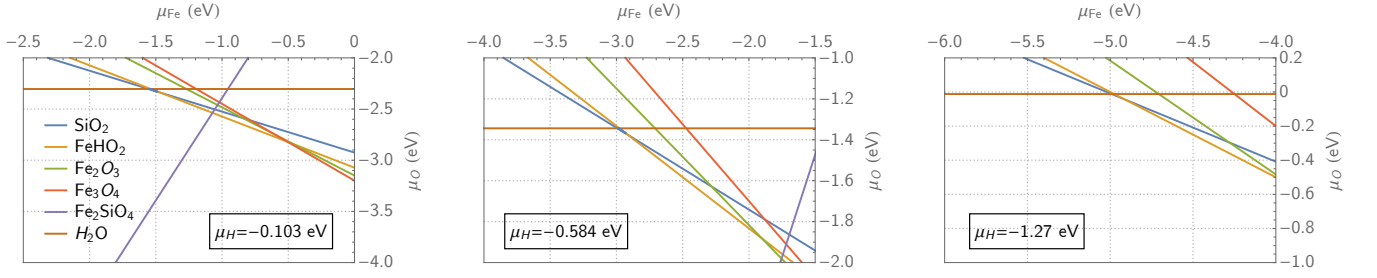


FIG. 4. Phase diagrams for $\text{Fe}_2\text{Si}_2\text{O}_9\text{H}_4$: a) hydrogen chemical potential μ_H is set to -0.103 eV, b) μ_H is set to -0.584 eV and c) μ_H is set to -1.27 eV. Stability regions are shaded in blue.

$\text{Fe}_3\text{Si}_2\text{O}_9\text{H}_4$ and $\text{Fe}_2\text{Si}_2\text{O}_9\text{H}_4$ are isolated 2D layers, but their energetics is competing against bulk compounds. The iron silicate can be further stabilized trivially by considering its bulk version, but more relevantly by placing it on a substrate for added stabilization from the wetting (binding) energy to the substrate. Such an added binding energy would increase the stability region in Fig. 4 as the SiO_2 and Fe_2SiO_4 curves would shift down with the increased formation energy of the $\text{Fe}_{2,3}\text{Si}_2\text{O}_9\text{H}_4$ while the curves for all the other iron oxides and FeHO_2 remains fixed at constant μ_H .

various substrates but without hydrogen [18]. Those films were found to be chemically bonded to substrates; because they are intrinsically electron deficient, the substrates transfers electrons to the film. Providing hydrogen that will bind to the silicate (e.g., via a hydrogen plasma in experiments) can provide the needed electrons to the film instead. This may then weaken the substrate binding and permit exfoliation. While hydrogen migration on a substrate can be more complex than what we analyze here, our results provide guidance for what may happen on a substrate.

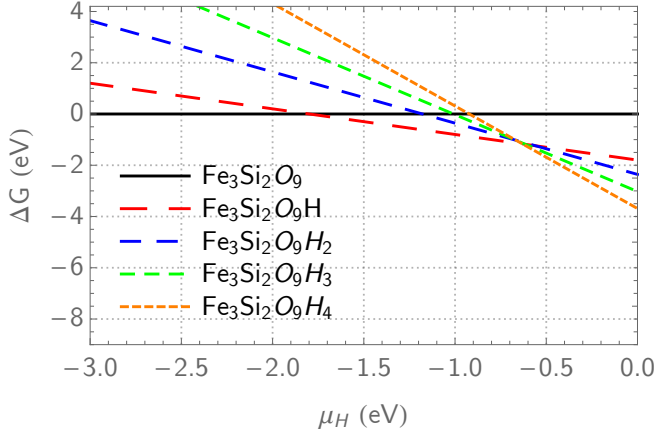
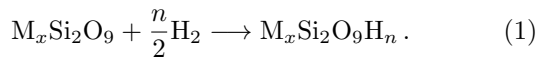


FIG. 5. Gibbs free energy, ΔG , of the hydrogenation reaction of Eq. (1) for $\text{Fe}_3\text{Si}_2\text{O}_9\text{H}_n$ as a function of the chemical potential of hydrogen, μ_H .

In Fig. 5 and and 6, we show the Gibbs free energy of hydrogenation for the following chemical reaction,



We note that these curves only indicate the relative stability of each compound, not the thermodynamic stability of the compound which is determined through hull energies in Table I. This reaction only describes whether hydrogenation of the transition metal silicates is thermodynamically favorable. Previous experiments showed the formation of transition metal silicates on

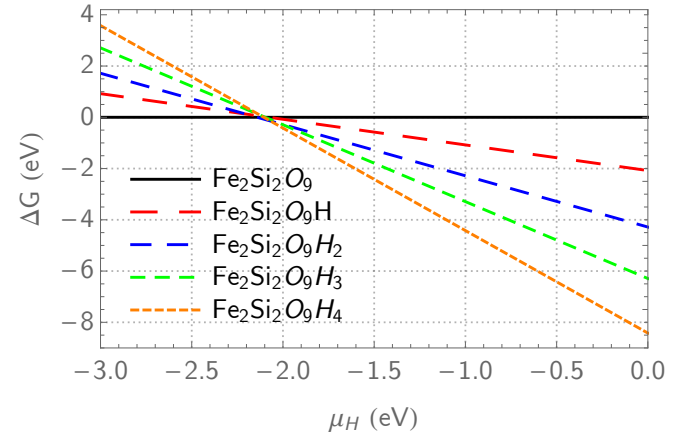


FIG. 6. Gibbs free energy, ΔG , for Eq. (1) and $\text{Fe}_2\text{Si}_2\text{O}_9\text{H}_n$ as a function of the chemical potential of hydrogen.

Among the hydroxylated phases of $\text{Fe}_3\text{Si}_2\text{O}_9\text{H}_n$, only $\text{Fe}_3\text{Si}_2\text{O}_9\text{H}$ and $\text{Fe}_3\text{Si}_2\text{O}_9\text{H}_4$ are relatively stable compared to the others which can be explained through the valence state of the Fe atoms. In $\text{Fe}_3\text{Si}_2\text{O}_9\text{H}$, all the Fe atoms are in the 3+ state, whereas in $\text{Fe}_3\text{Si}_2\text{O}_9\text{H}_4$ all the Fe atoms are in 2+ state. Hence, we can conclude that under increasingly H-rich conditions, the charge disproportionation in the Fe atoms is expected to disappear.

In Fig. 6, we show the same analysis for $\text{Fe}_2\text{Si}_2\text{O}_9\text{H}_n$ and find that, essentially, a transition only occurs between $\text{Fe}_2\text{Si}_2\text{O}_9$ and $\text{Fe}_2\text{Si}_2\text{O}_9\text{H}_4$ compounds. This can be understood in a similar way as in 5. In $\text{Fe}_2\text{Si}_2\text{O}_9$, all Fe atoms are in the 5+ state, and in $\text{Fe}_2\text{Si}_2\text{O}_9\text{H}_4$ they

reduce to the 3+ state. Given that Fe would prefer oxidation states with 2+ and 3+, there is no intermediate hydrogenated compound that is stable. Additionally, in Fig. 6, the transition occurs at a similar chemical potential to the first transition in Fig. 5, but much lower than the second transition in Fig. 5 where complete hydrogenation has occurred. This implies that it is significantly easier to obtain a completely hydrogenated 2D Fe-silicate with the kaolinite-like structure once the base compound is formed.

2. Cr-silicates

Our analysis of Cr-silicates and the remaining the silicates will follow closely our analysis of Fe-silicates. In Table II, we present our data on Cr-silicates in the same manner as the Fe-silicates in Table I. Hull energies in Table II are determined using a Cr-Si-O-H quaternary phase diagram using the compounds listed in the supplementary information [53]. The only stable compound in Table II is $\text{Cr}_2\text{Si}_2\text{O}_9\text{H}_4$. There is a clear trend of increasing stability with increased hydrogenation in nontronites and kaolinites, but for lizardites the trend is in the opposite direction. This may be because, in lizardites, increased hydrogenation yields the 2+ charge state Cr, which is energetically unfavorable compared to 3+ state.

TABLE II. Average oxidation number of the Cr atoms, N_{ox}^{Cr} , electronic configuration (EC) of the Cr atoms are given for each compound. Calculated formation enthalpies, E_f , distance to convex hull, E_{hull} , (both are given in eV/atom) are shown. Average magnetic moment per Cr-atom in the high-spin FM state is given in μ_B/atom .

Material	N_{ox}^{Cr}	EC	E_f	E_{hull}	μ_M
<i>Nontronites</i>					
$\text{Cr}_2\text{Si}_2\text{O}_8$	4+	d^2	-2.553	0.057	2.19
$\text{Cr}_2\text{Si}_2\text{O}_8\text{H}$	3.5+	d^2, d^3	-2.428	0.113	2.55
$\text{Cr}_2\text{Si}_2\text{O}_8\text{H}_2$	3+	d^3	-2.312	0.17	2.96
<i>Kaolinites</i>					
$\text{Cr}_2\text{Si}_2\text{O}_9$	5+	d^1	-2.368	0.041	1.43
$\text{Cr}_2\text{Si}_2\text{O}_9\text{H}$	4.5+	d^1, d^2	-2.315	0.045	1.94
$\text{Cr}_2\text{Si}_2\text{O}_9\text{H}_2$	4+	d^2	-2.280	0.036	2.32
$\text{Cr}_2\text{Si}_2\text{O}_9\text{H}_3$	4.5+	d^2, d^3	-2.235	0.019	2.71
$\text{Cr}_2\text{Si}_2\text{O}_9\text{H}_4$	3+	d^3	-2.201	0	2.96
<i>Lizardites</i>					
$\text{Cr}_3\text{Si}_2\text{O}_9$	3.33+	d^2, d^3	-2.621	0.032	2.83
$\text{Cr}_3\text{Si}_2\text{O}_9\text{H}$	3+	d^3	-2.545	0.046	2.98
$\text{Cr}_3\text{Si}_2\text{O}_9\text{H}_2$	2.67+	d^3, d^4	-2.346	0.083	3.36
$\text{Cr}_3\text{Si}_2\text{O}_9\text{H}_3$	2.34+	d^3, d^4	-2.170	0.116	3.68
$\text{Cr}_3\text{Si}_2\text{O}_9\text{H}_4$	2+	d^4	-2.027	0.132	3.75

The stability diagram for $\text{Cr}_2\text{Si}_2\text{O}_9\text{H}_4$ is provided in the supplementary information. Similar to $\text{Fe}_2\text{Si}_2\text{O}_9\text{H}_4$ in Fig. 4, the stability region of $\text{Cr}_2\text{Si}_2\text{O}_9\text{H}_4$ is bounded

by H_2O , SiO_2 and CrHO_2 . When constructing Cr-Si-O-H phase diagram, our search did not yield a thermodynamically stable Cr-Si-O ternary compound, unlike Fe_2SiO_4 . The corresponding Cr_2SiO_4 structure has been synthesized only at elevated temperatures with rapid quenching [55], and it is reported to be metastable within DFT [56], suggesting that the structure can only be kinetically trapped. We find that the Gibbs free energy of hydrogenation of $\text{Cr}_2\text{Si}_2\text{O}_9\text{H}_4$, given in supplementary information, is similar to the hydrogenation of $\text{Fe}_2\text{Si}_2\text{O}_9\text{H}_4$ in Fig. 6. The main difference between the hydrogenation of two materials is that the energetic crossing between $\text{Cr}_2\text{Si}_2\text{O}_9$ and $\text{Cr}_2\text{Si}_2\text{O}_9\text{H}_4$ occurs at a larger chemical potential compared to $\text{Fe}_2\text{Si}_2\text{O}_9\text{H}_4$. This agrees with the fact that Fe has a larger ionization potential compared to Cr, hence hydrogenation is comparatively more favorable at lower hydrogen availability.

3. Mn-silicates

Table III shows that none of the Mn-silicates are found to be stable in the Mn-Si-O-H phase diagram we constructed using the compounds given in supplementary information. Nevertheless, similar trends are observed as in Cr and Fe-silicates, such that increased hydrogenation typically stabilizes the compound. This trend is more obvious in $\text{Mn}_2\text{Si}_2\text{O}_9\text{H}_n$, where Mn transitions from being 5+ to 3+ with increased hydrogenation. However, for $\text{Mn}_3\text{Si}_2\text{O}_9\text{H}_n$, cases where Mn has an integer oxidation state of 3+ or 2+ are more stable compared to fractional oxidation states. We find that $\text{Mn}_3\text{Si}_2\text{O}_9\text{H}_n$ favors the 3+ oxidation state only slightly more than the 2+ state, which is expected given that these two oxidation states are the most commonly observed for Mn compounds [ref here].

TABLE III. Ground state properties of 2D Mn-silicates

Material	N_{ox}^{Mn}	EC	E_f	E_{hull}	μ_M
<i>Nontronites</i>					
$\text{Mn}_2\text{Si}_2\text{O}_8$	4+	d^3	-2.375	0.172	
$\text{Mn}_2\text{Si}_2\text{O}_8\text{H}$	3.5+	d^2, d^3	-2.317	0.125	
$\text{Mn}_2\text{Si}_2\text{O}_8\text{H}_2$	3+	d^4	-2.256	0.095	
<i>Kaolinites</i>					
$\text{Mn}_2\text{Si}_2\text{O}_9$	5+	d^2	-2.122	0.169	3.02
$\text{Mn}_2\text{Si}_2\text{O}_9\text{H}$	4.5+	d^2, d^3	-2.158	0.114	3.06
$\text{Mn}_2\text{Si}_2\text{O}_9\text{H}_2$	4+	d^3	-2.172	0.032	3.16
$\text{Mn}_2\text{Si}_2\text{O}_9\text{H}_3$	3.5+	d^3, d^4	-2.126	0.018	3.54
$\text{Mn}_2\text{Si}_2\text{O}_9\text{H}_4$	3+	d^4	-2.069	0.013	3.87
<i>Lizardites</i>					
$\text{Mn}_3\text{Si}_2\text{O}_9$	3.33+	d^3, d^4	-2.467	0.038	3.92
$\text{Mn}_3\text{Si}_2\text{O}_9\text{H}$	3+	d^4	-2.391	0.026	3.93
$\text{Mn}_3\text{Si}_2\text{O}_9\text{H}_2$	2.67+	d^4, d^5	-2.274	0.046	4.27
$\text{Mn}_3\text{Si}_2\text{O}_9\text{H}_3$	2.34+	d^4, d^5	-2.168	0.045	4.44
$\text{Mn}_3\text{Si}_2\text{O}_9\text{H}_4$	2+	d^5	-2.088	0.031	4.63

We study the hydrogenation of Mn-silicates using Eq. 1 and show the associated figures in the supplementary information. We find the same relation between the Gibbs free energy of hydrogenations in $\text{Mn}_3\text{Si}_2\text{O}_9\text{H}_n$ and $\text{Fe}_3\text{Si}_2\text{O}_9\text{H}_n$ in Fig. 5. The only difference is that the hydrogen chemical potentials at the transition points for $\text{Mn}_3\text{Si}_2\text{O}_9\text{H}_n$ are higher compared to $\text{Fe}_3\text{Si}_2\text{O}_9\text{H}_n$, which is a similar trend we noted for Cr-silicates. For $\text{Mn}_2\text{Si}_2\text{O}_9\text{H}_n$, however, there is an additional regions of hydrogen chemical potential where $\text{Mn}_3\text{Si}_2\text{O}_9\text{H}$ and $\text{Mn}_3\text{Si}_2\text{O}_9\text{H}_2$ are stable as well. This is in contrast to the Fe-silicates where we have a direct transition from $\text{Fe}_3\text{Si}_2\text{O}_9$ to $\text{Fe}_3\text{Si}_2\text{O}_9\text{H}_4$ in Fig. 6. This may be because Mn tends to commonly accept a wider range of oxidation states compared to Fe, therefore the differences between higher degrees of ionization energies should be small enough to allow stepwise hydrogenation as opposed to the Fe-silicate examples.

4. Co-silicates

Table IV shows that the stability trends for Co-silicates are very similar to those in Table I. Again, the stability increases with increased hydrogenation and hull energies of trioctahedral Co-silicates are consistently smaller than dioctahedral derivatives. Similarly, we find that the stability regions of $\text{Co}_3\text{Si}_2\text{O}_9\text{H}_4$ are larger than $\text{Co}_2\text{Si}_2\text{O}_9\text{H}_4$ (see the supplementary information). An important difference between the Co and Fe-silicates is that $\text{Co}_2\text{Si}_2\text{O}_9\text{H}_4$ starts forming at a lower hydrogen chemical potential than for $\text{Fe}_{(2,3)}\text{Si}_2\text{O}_9\text{H}_4$ silicates. Given that the stability region is mainly determined by SiO_2 , CoHO_2 and H_2O curves, this can be explained by the fact that the CoHO_2 formation enthalpy is significantly higher than FeHO_2 (1.13 eV vs 1.56 eV). Compared to FeHO_2 , CoHO_2 is less likely to form.

We study the hydrogenation of Co-silicates using Eq. 1 and show the plots in the supplementary information. In $\text{Co}_3\text{Si}_2\text{O}_9\text{H}_4$, we find that Gibbs free energy of hydrogenation has the following trend going from Fe to Mn and Co. In $\text{Fe}_3\text{Si}_2\text{O}_9\text{H}_n$ (Fig. 5), the hydrogenation is stepwise such that after $\text{Fe}_3\text{Si}_2\text{O}_9$, first $\text{Fe}_3\text{Si}_2\text{O}_9\text{H}$ and then $\text{Fe}_3\text{Si}_2\text{O}_9\text{H}_4$ is formed. $\text{Mn}_3\text{Si}_2\text{O}_9\text{H}_4$ is similar to this but the range of stability for $\text{Mn}_3\text{Si}_2\text{O}_9\text{H}$ is smaller compared to $\text{Fe}_3\text{Si}_2\text{O}_9\text{H}$. Following this trend, the range of stability for $\text{Co}_3\text{Si}_2\text{O}_9\text{H}$ disappears completely (we will see that the range of stability for $\text{Ni}_3\text{Si}_2\text{O}_9\text{H}$ is again smaller compared to $\text{Fe}_3\text{Si}_2\text{O}_9\text{H}$ and $\text{Mn}_3\text{Si}_2\text{O}_9\text{H}$). Gibbs free energy of hydrogenation curves for $\text{Co}_2\text{Si}_2\text{O}_9\text{H}_n$ are similar to $\text{Fe}_2\text{Si}_2\text{O}_9\text{H}_n$ except that the μ_H at the transition point for $\text{Co}_2\text{Si}_2\text{O}_9\text{H}_n$ is slightly smaller.

5. Ni-silicates

In Table V we observe trends in stability that are very similar to Table I. Again, the stability increases with

TABLE IV. Ground state properties of 2D Co-silicates

Material	N_{ox}^{Co}	EC	E_f	E_{hull}	μ_M
<i>Nontronites</i>					
$\text{Co}_2\text{Si}_2\text{O}_8$	4+	d ⁵	-2.078	0.091	
$\text{Co}_2\text{Si}_2\text{O}_8\text{H}$	3.5+	d ⁶ , d ⁵	-2.059	0.049	
$\text{Co}_2\text{Si}_2\text{O}_8\text{H}_2$	3+	d ⁶	-2.028	0.028	
<i>Kaolinites</i>					
$\text{Co}_2\text{Si}_2\text{O}_9$	5+	d ⁴	-1.924	0.078	2.58
$\text{Co}_2\text{Si}_2\text{O}_9\text{H}$	4.5+	d ⁴ , d ⁵	-1.865	0.092	2.25
$\text{Co}_2\text{Si}_2\text{O}_9\text{H}_2$	4+	d ⁵	-1.868	0.050	2.05
$\text{Co}_2\text{Si}_2\text{O}_9\text{H}_3$	3.5+	d ⁵ , d ⁶	-1.861	0.020	2.78
* $\text{Co}_2\text{Si}_2\text{O}_9\text{H}_4$	3+	d ⁶	-1.847	0.000	3.15
<i>Lizardites</i>					
$\text{Co}_3\text{Si}_2\text{O}_9$	3.33+	d ⁵	-2.049	0.036	2.07
$\text{Co}_3\text{Si}_2\text{O}_9\text{H}$	3+	d ⁵ , d ⁶	-2.003	0.036	3.01
$\text{Co}_3\text{Si}_2\text{O}_9\text{H}_2$	2.67+	d ⁶	-1.958	0.033	2.99
$\text{Co}_3\text{Si}_2\text{O}_9\text{H}_3$	2.34+	d ⁶ , d ⁷	-1.932	0.010	2.87
* $\text{Co}_3\text{Si}_2\text{O}_9\text{H}_4$	2+	d ⁷	-1.899	0.000	2.74

increased hydrogenation and hull energies of trioctahedral Ni-silicates are consistently smaller than dioctahedral derivatives. However, the hull energy of $\text{Ni}_2\text{Si}_2\text{O}_9$ is larger compared to $\text{Fe}_2\text{Si}_2\text{O}_9$, whereas the hull energy of $\text{Ni}_3\text{Si}_2\text{O}_9$ is smaller than $\text{Fe}_3\text{Si}_2\text{O}_9$. This indicates that overall, Ni-silicates have stronger tendency to form trioctahedral compounds compared to Fe-silicates. This is to be expected: Ni commonly has an oxidation state of 2+ unlike Mn, Fe and Co which are more commonly found in 2+ and 3+ oxidation states. Similarly, we had found that the only stable Cr-silicate in our work is $\text{Cr}_2\text{Si}_2\text{O}_9\text{H}_4$, where Cr has an oxidation state of 3+ in the dioctahedral form. In $\text{Ni}_3\text{Si}_2\text{O}_9\text{H}_4$, Ni prefers an oxidation state of 2+ in the trioctahedral form. Hence, it can be argued that for Mn-Co silicates dioctahedral and trioctahedral phases are in competition and coexist, but for Cr and Ni silicates one phase is clearly favored over the other.

We study the hydrogenation of Ni-silicates using Eq. 1 and show the data in the supplementary information. Hydrogenation of $\text{Ni}_3\text{Si}_2\text{O}_9\text{H}_n$ follows the same trend that we discussed in $\text{Co}_3\text{Si}_2\text{O}_9\text{H}_n$. There is a stability range for $\text{Ni}_3\text{Si}_2\text{O}_9\text{H}$ that exists, but it is much smaller compared to $\text{Mn}_3\text{Si}_2\text{O}_9\text{H}$ and $\text{Fe}_3\text{Si}_2\text{O}_9\text{H}$.

B. Magnetic structure

In Table VI, we compare antiferromagnetic (AFM) and ferromagnetic (FM) phases of kaolinites and lizardites. Kaolinites have a honeycomb lattice in the M-O layer (see Fig. 1b), hence we considered the G-type (checkerboard) AFM ordering using the primitive cell of this material. In Lizardites, however, we calculate a striped AFM ordering using a rectangular supercell with 2 S_0 surface area, where S_0 is the surface area of the primitive cell.

TABLE V. Ground state properties of 2D Ni-silicates

Material	N_{ox}^{Ni}	EC	E_f	E_{hull}	μ_M
<i>Nontronites</i>					
$Ni_2Si_2O_8$	4+	d^6	-1.709	0.256	
$Ni_2Si_2O_8H$	3.5+	d^6, d^7	-1.761	0.187	
$Ni_2Si_2O_8H_2$	3+	d^7	-1.797	0.135	
<i>Kaolinites</i>					
$Ni_2Si_2O_9$	5+	d^5	-1.511	0.304	1.29
$Ni_2Si_2O_9H$	4.5+	d^5, d^6	-1.579	0.264	1.61
$Ni_2Si_2O_9H_2$	4+	d^6	-1.571	0.232	2.12
$Ni_2Si_2O_9H_3$	3.5+	d^6, d^7	-1.671	0.170	2.14
* $Ni_2Si_2O_9H_4$	3+	d^7	-1.647	0.110	2.16
<i>Lizardites</i>					
$Ni_3Si_2O_9$	3.33+	d^6, d^7	-1.756	0.069	1.33
$Ni_3Si_2O_9H$	3+	d^7	-1.788	0.030	1.40
$Ni_3Si_2O_9H_2$	2.67+	d^7, d^8	-1.792	0.021	1.54
$Ni_3Si_2O_9H_3$	2.34+	d^7, d^8	-1.774	0.034	1.66
$Ni_3Si_2O_9H_4$	2+	d^8	-1.804	0.000	1.80

Although larger supercells will allow for more complex magnetic ordering patterns, here we restrict ourselves to these simple orderings to obtain an overall assessment of the magnetic ordering energy scales at reasonable computational costs: to understand the potential of these structures as possible FM 2D layers, comparing simple FM and AFM orderings can provide a good estimate.

TABLE VI. Magnetic properties of transition metal silicates

Material	$E_{AFM} - E_{FM}$ (meV per metal atom)
<i>Kaolinites</i>	
$Cr_2Si_2O_9H_4$	3
$Mn_2Si_2O_9H_4$	-8
$Fe_2Si_2O_9H_4$	-3
$Co_2Si_2O_9H_4$	-28
$Ni_2Si_2O_9H_4$	-201
<i>Lizardites</i>	
$Mn_3Si_2O_9H_4$	-24
$Fe_3Si_2O_9H_4$	-1
$Co_3Si_2O_9H_4$	1
$Ni_3Si_2O_9H_4$	-2

Our results in Table VI show that the energy differences between the AFM and FM phases are mostly quite small, and that the ground state is mainly AFM. For many, the small AFM-FM energy difference means no magnetic ordering is likely at room temperature; for $Co_2Si_2O_9H_4$, $Mn_3Si_2O_9H_4$ and $Ni_2Si_2O_9H_4$ the AFM order is expected to survive at or near room temperature. We note that $Ni_2Si_2O_9H_4$ in Table VI is a thermodynamically unstable structure since each Ni atom has a 3+ oxidation state. Similarly, $Cr_3Si_2O_9H_4$ is also a

thermodynamically unstable material and given then Cr atoms would have a 2+ oxidation state in this structure. In the supplementary material [53], we show that the same conclusion can also be made for $Cr_3Si_2O_9H_4$.

The main FM candidate in Table VI is the kaolinite $Cr_2Si_2O_9H_4$, although the Curie temperature is likely to be very low. This is similar to the magnetism in Cr-Ni pyroxenes which yields an AFM ground state for Mn to Fe-pyroxenes [57, 58] but a FM ground state for Cr-pyroxenes. Pyroxenes and kaolinites are structurally rather similar. In both structures the magnetism is mediated over M-O-M bonds which are close to 90°. In pyroxenes, however, M-O octahedra form one dimensional chains which are separated by alkali atoms such as Li and Na, as opposed to the two-dimensional M-O layer in kaolinites. In Cr-pyroxenes, it was shown that the AFM t_{2g} - t_{2g} exchange interaction is nearly compensated by the FM t_{2g} - e_g exchange, but fine-tuning of these interactions is possible via the size of the alkali atom [57]. In $NaCrGe_2O_6$, the largest Cr-Cr separation was observed which yields a FM structure [57]. Although not examined here, future work can examine if it is possible to incorporate additional transition metal atoms in the vacancies of the honeycomb lattice of Cr-kaolinite to increase FM coupling and/or have a ferrimagnetic ground state with a net magnetization.

As we previously discussed, greenalite, $Fe_{2,3}Si_2O_9H_4$, is observed to be ferromagnetic in the plane with an intraplane magnetic coupling constant of 15 K [28]. Fe sites in greenalite are disordered however, meaning that some octahedral sites are filled with Fe, whereas others are hollow. In this perspective, greenalite can be considered a solid solution of the ordered Fe-kaolinite and Fe-lizardite phases we studied. However, our calculations do not yield a ferromagnetic order in these ordered lizardite and kaolinite phases. For Fe-silicates, our calculations yield a checkerboard AFM phase for $Fe_2Si_2O_9H_4$ and striped AFM phase for $Fe_3Si_2O_9H_4$ as the stable phase compared to FM phases. Therefore, we can understand that the ferromagnetism of greenalite is correlated to the disorder in its structure. Similar accounts of enhanced ferromagnetism with increased disorder were reported in 3D alloys [59] as well as disordered and doped 2D-materials [60, 61]. As we predict both lizardite and kaolinite Fe-silicates to be thermodynamically stable, synthesis conditions might be engineered to make partially occupied Fe-O layer which can yield magnetic properties similar to greenalite.

C. Piezoelectric properties

Here, we describe the piezoelectric properties of the thermodynamically stable 2D silicates identified above. Both kaolinites and the lizardites have symmetry point groups that do not include inversion, hence they are expected to have a finite piezoelectric response under strain or electric field. We use the following standard relations

to calculate the elastic modulus tensor C_{ij} and piezoelectric strain tensor $e_{\alpha j}$:

$$\begin{aligned}
 C_{ij} &= \frac{d\sigma_i}{d\eta_j}, \\
 e_{\alpha j} &= \frac{dP_\alpha}{d\eta_j} = e_{\alpha j,c} + e_{\alpha j,i} \\
 e_{\alpha j,c} &= \left. \frac{\partial P_\alpha}{\partial \eta_j} \right|_u = \left. \frac{\partial^2 E}{\partial \mathcal{E}_\alpha \partial \eta_j} \right|_u, \\
 e_{\alpha j,i} &= \sum_m \frac{\partial P_\alpha}{\partial u_m} \frac{\partial u_m}{\partial \eta_j}, \\
 d_{\alpha j} &= \frac{dP_\alpha}{d\sigma_j} = \sum_i e_{\alpha i} \cdot (C^{-1})_{ji}.
 \end{aligned} \tag{2}$$

Here, σ_i is the stress tensor, η_j is the strain tensor, $e_{\alpha j}$ is the piezoelectric tensor with subscripts i and c denoting the ionic and clamped ion components respectively, E is the total energy of the system, \mathcal{E}_α is the imposed electric field vector, u are the atomic displacements from equilibrium, $d_{\alpha j}$ is the piezoelectric strain tensor, and P_α is the polarization vector. Greek indices such as α represent axis directions and Latin indices such as i, j describe tensor components using Voigt notation.

We apply a symmetry and dimensionality analysis to define in-plane directions and independent components of the elastic and piezoelectric tensors. Plane-wave based DFT codes such as VASP calculate the C_{ij} and $e_{\alpha j}$ constants based on periodic boundary conditions of a 3D system. Therefore, it is important that these quantities are modified or converted for a 2D case with in-plane stress and strain. For a 2D system, this means that the σ_i and ϵ_j are zero when i or j involves the out-of-plane z direction [8, 9]. Also, a renormalization is needed for the elastic and strain tensors such that $C_{ij}^{2D} = a_z \cdot C_{ij}^{3D}$ and $e_{ij}^{2D} = a_z \cdot e_{ij}^{3D}$, where a_z is the length of the simulation cell in z -direction. However, the polarization P_α is not restricted to remain in-plane.

We use orthorhombic simulation cells for both lizardite and kaolinite derivatives to calculate elastic and piezoelectric constants as defined in the SI [53]. In these cells, the in-plane lattice parameters along the x -axes were chosen to be longer than the lattice parameters on y -axes. In all structures, the z -direction is perpendicular to the xy -plane. Lizardites have the $3m$ point-group symmetry, hence x and y in-plane directions are identical [8, 9]. However, the honeycomb lattice of kaolinites leads to an anisotropy between x and y directions, which was previously noted by Sato et. al. [62]. Since 2D kaolinite and lizardite crystals have the m and $3m$ point group symmetries respectively, the complete piezoelectric strain tensor can be obtained using only the independent tensor elements. For $3m$ point group symmetry, these are $e_{22} = e_{21} = e_{16}$ and $e_{32} = e_{31}$ and in m point group symmetry these are e_{21} , e_{22} , e_{31} , e_{32} and e_{16} [63]. In both structures, $e_{11} = e_{12} = 0$.

In Tables VIII and VII, we show that the elastic properties of transition metal silicates are very similar to each

other. The main difference is that elastic constants of kaolinites are smaller than the lizardites. This is most likely because the hexagonal vacancy in kaolinites allows additional room for relaxation, leading to smaller the elastic moduli. Indeed, a similar conclusion can be made using the bulk forms of kaolinite and lizardite (3D $\text{Al}_2\text{Si}_2\text{O}_9\text{H}_3$ and $\text{Mg}_3\text{Si}_2\text{O}_9\text{H}_3$, respectively) where C_{11} elastic constants of 200 and 245 GPa were calculated using DFT, respectively [62, 64]. Additionally, the C_{11} elastic constant of kaolinites tend to decrease from Cr- to Ni-kaolinite, whereas in lizardites the trend is the opposite. This can be related to the trends in structural parameters. We find that the average volume of the transition metal octahedra and the in-plane surface area decreases going from Mn to Ni in both structures. This can be related to reduced atomic size going towards Ni, hence more tightly packed structures and larger elastic constants for lizardites. We have excluded Cr-kaolinite in these trends because Cr-kaolinite has no e_g electrons, hence a smaller valence shell, and therefore shorter Cr-O bonds.

In Tables VIII and VII, piezoelectric and elastic tensor components are reported. General trends we find in these tables are the following: In both structures, clamped-ion and relaxed ion piezoelectric constants, e_{ij} , differ dramatically and lead to a change of sign in e_{31}/e_{32} . We should mention that the sign of the e_{31}/e_{32} piezoelectric constants are relative to the orientation of the 2D layer, i.e. whether the silicate layer is on top of the transition metal oxide layer. We kept the orientation of layers fixed in all our calculations such that transition metal oxide layer is always on top. This change of sign was also observed in the e_{33} constants of 3D auxetic piezoelectric crystals and vdW solids [65, 66] and it was found that the magnitude of the ionic contribution is typically much larger than the magnitude of the clamped-ion contribution in these auxetic materials. In ref. 66, it was pointed out that this large ionic contribution is a main character of auxetic piezoelectric materials and both e_{31} and e_{33} constants are both of negative sign. In quasi-2D materials, e_{33} constants can be obtained experimentally [67], but this is challenging for the computational methods. In the SI [53], we further discuss this issue, but we find that even by using Density Functional Perturbation Theory (DFPT) [68], the internal strain tensor basically corresponds to some uniform scaling along the z -axes, hence the e_{33} constants can be obtained using only the born effective charges. Thus, we have not yet identified a rigorous way to calculate the e_{33} constants of quasi-2D materials. Similar to e_{31}/e_{32} constants, we find that the e_{22} constants in both materials differ significantly between the clamped-ion and relaxed-ion conditions. However, similar observation for the in-plane piezoelectric constants were previously made on a diverse set of 2D materials and found to be related to their mechanical softness and ionic relaxation in out-of-plane directions [69]. In kaolinites, we find that d_{31} are larger than d_{32} constants in magnitude, which can be

TABLE VII. Elastic coefficients (C_{ij}) and piezoelectric coefficients (e_{ij} and d_{ij}) of 2D kaolinites. $C_{12} = C_{21}$, whereas e_{11} and e_{12} are zero due to the symmetry.

	<i>clamped-ion</i>				<i>relaxed-ion</i>											
	e21	e22	e31	e32	C11	C12	C22	C66	e21	e22	e31	e32	d21	d22	d31	d32
	pC/m				N/m				pC/m				pm/V			
Cr2Si2O9H4	-6.5	-3.5	26.0	38.1	148.9	54.4	132.2	32.8	40.9	68.9	-39.3	-23.9	0.10	0.48	-0.23	-0.08
Mn2Si2O9H4	1.6	-6.7	30.7	41.2	141.1	49.8	125.7	25.8	83.8	82.3	-54.8	-36.9	0.42	0.49	-0.33	-0.16
Fe2Si2O9H4	-7.6	-1.6	24.4	40.3	143.4	52.9	123.9	29.3	41.4	132.0	-40.2	-21.0	0.12	1.11	-0.26	-0.06
Co2Si2O9H4	6.9	-4.7	27.2	38.1	141.5	48.9	117.8	23.8	53.7	53.8	-40.9	-20.2	0.26	0.35	-0.27	-0.06
Ni2Si2O9H4	1.2	8.2	28.4	39.8	138.2	48.3	113.8	29.3	83.1	56.3	-45.2	-24.1	0.50	0.29	-0.29	-0.10

TABLE VIII. Elastic coefficients (C_{ij}) and piezoelectric coefficients (e_{ij} and d_{ij}) of 2D lizardites. $C_{12} = C_{21}$, $C_{11} = C_{22}$, $e_{21} = e_{22}$ and $e_{31} = e_{32}$, whereas e_{11} and e_{12} are zero due to symmetry.

	<i>clamped-ion</i>		<i>relaxed-ion</i>							
	e22	e32	C12	C22	C66	e22	e32	d22	d32	
	pC/m		N/m			pC/m		pm/V		
Mn3Si2O9H4	0.6	40.2	139.7	54.9	42.0	69.4	-21.5	0.82	-0.11	
Fe3Si2O9H4	2.1	42.9	139.0	55.3	41.7	12.8	-35.7	0.15	-0.18	
Co3Si2O9H4	3.1	41.5	148.0	62.3	43.8	39.3	-27.2	0.46	-0.13	
Ni3Si2O9H4	4.9	36.3	161.8	64.7	48.1	32.2	-35.8	0.33	-0.16	

correlated to a similar difference in e_{31} and e_{32} constants as a result of the anisotropy observed in these materials. Similarly, d_{32} constants in kaolinites are typically smaller than that of lizardites, however, d_{31} constants in each material (in lizardites $d_{31} = d_{32}$) are comparable. The d_{3j} constants we found in tables VIII and VII are all smaller than 1 pm/V, which is on par with most quasi-2D materials which all have d_{31} smaller than 1 pm/V, such as Janus-type transition metal dichalcogenides [70], buckled hexagonal III-V compounds [8], and doped graphene [71].

We find that the main contribution to the relaxed ion piezoelectric constants, $e_{\alpha j, i}$, comes from the displacements of the Si and O atoms in the SiO_4 tetrahedra in these structures, which explains relatively similar performance across different substituents [53]. We analyze the atomic displacements due to strain that contribute to $e_{\alpha j, i}$ using the tensor $A_{mj} = \partial u_m / \partial \eta_j$ in the SI [53]. We find that SiO_4 tetrahedra move closer to the MO_6 layer with tensile strain as would be expected from a material with a positive Poisson ratio. Strain in the x ($\equiv 1$) direction induces displacements in the Si-O bond between the SiO_4 tetrahedra and the MO_6 layer such that Si and O atoms in the SiO_4 tetrahedra move up or down collectively. The magnitude of displacements in these atoms are larger compared to the rest of the system.

IV. CONCLUSION

In conclusion, we present detailed theoretical investigation of the thermodynamic, electronic, magnetic and

piezoelectric properties of 2D transition metal silicates, $\text{M}_{2-3}\text{Si}_2\text{O}_9\text{H}_n$, where $n=(0,4)$. We showed that these materials can be thermodynamically stable with hydrogenation. Our ultimate goal is to create a material that can possess ferromagnetism ideally at elevated temperatures and also have piezoelectric properties, which can be coupled to each other to modulate multiferroic behavior. Although, the magnetic properties of these materials are predominantly antiferromagnetic or weak ferromagnetic at best, we expect that this materials framework and the facile experimental synthesis methods [18] allow further engineering of the transition metal layer, which can provide richer chemical phase space and magnetic ordering. Further work will follow on this aspect. Symmetry of these structures dictate that a finite piezoelectric response should exist, which is on par with a wide range of quasi-2D materials that show similar performance.

ACKNOWLEDGEMENT

We acknowledge the Army Research Office grant W911NF-19-1-0371 for the funding of this work and also the computational resources provided by the institutional clusters at Yale University.

-
- [1] K. S. Burch, D. Mandrus, and J.-G. Park, *Nature* **563**, 47 (2018).
- [2] M. Gibertini, M. Koperski, A. F. Morpurgo, and K. S. Novoselov, *Nat. Nanotechnol.* **14**, 408 (2019).
- [3] C. Gong, L. Li, Z. Li, H. Ji, A. Stern, Y. Xia, T. Cao, W. Bao, C. Wang, Y. Wang, Z. Q. Qiu, R. J. Cava, S. G. Louie, J. Xia, and X. Zhang, *Nature* **546**, 265 (2017).
- [4] G. Barcaro and A. Fortunelli, *Phys. Chem. Chem. Phys.* **21**, 11510 (2019).
- [5] H.-C. Cheng, G. Wang, D. Li, Q. He, A. Yin, Y. Liu, H. Wu, M. Ding, Y. Huang, and X. Duan, *Nano Lett.* **16**, 367 (2016).
- [6] K. S. Novoselov, A. Mishchenko, A. Carvalho, and A. H. Castro Neto, *Science* (80-.). **353** (2016), 10.1126/science.aac9439.
- [7] A. K. Geim and I. V. Grigorieva, *Nature* **499**, 419 (2013).
- [8] M. N. Blonsky, H. L. Zhuang, A. K. Singh, and R. G. Hennig, *ACS Nano* **9**, 9885 (2015).
- [9] K. A. N. Duerloo, M. T. Ong, and E. J. Reed, *J. Phys. Chem. Lett.* **3**, 2871 (2012).
- [10] B. Huang, G. Clark, E. Navarro-Moratalla, D. R. Klein, R. Cheng, K. L. Seyler, D. Zhong, E. Schmidgall, M. A. McGuire, D. H. Cobden, W. Yao, D. Xiao, P. Jarillo-Herrero, and X. Xu, *Nature* **546**, 270 (2017).
- [11] Y. Zhou, D. Wu, Y. Zhu, Y. Cho, Q. He, X. Yang, K. Herrera, Z. Chu, Y. Han, M. C. Downer, H. Peng, and K. Lai, *Nano Lett.* **17**, 5508 (2017).
- [12] F. Liu, L. You, K. L. Seyler, X. Li, P. Yu, J. Lin, X. Wang, J. Zhou, H. Wang, H. He, S. T. Pantelides, W. Zhou, P. Sharma, X. Xu, P. M. Ajayan, J. Wang, and Z. Liu, *Nat. Commun.* **7**, 12357 (2016).
- [13] A. Belianinov, Q. He, A. Dziazgys, P. Maksymovych, E. Eliseev, A. Borisevich, A. Morozovska, J. Banys, Y. Vysochanskii, and S. V. Kalinin, *Nano Lett.* **15**, 3808 (2015).
- [14] Y. Tian, M. J. Gray, H. Ji, R. J. Cava, and K. S. Burch, *2D Mater.* **3**, 25035 (2016).
- [15] X. Wang, K. Du, Y. Y. F. Liu, P. Hu, J. Zhang, Q. Zhang, M. H. S. Owen, X. Lu, C. K. Gan, P. Sengupta, C. Kloc, and Q. Xiong, *2D Mater.* **3**, 31009 (2016).
- [16] N. Cabrera and N. F. Mott, *Reports Prog. Phys.* **12**, 163 (1949).
- [17] R. Włodarczyk, J. Sauer, X. Yu, J. A. Boscoboinik, B. Yang, S. Shaikhutdinov, and H. J. Freund, *J. Am. Chem. Soc.* **135**, 19222 (2013).
- [18] C. Zhou, X. Liang, G. S. Hutchings, Z. S. Fishman, J.-H. Jhang, M. Li, U. D. Schwarz, S. Ismail-Beigi, and E. I. Altman, *Chem. Mater.* **31**, 851 (2019).
- [19] F. D. Fischer, J. Sauer, X. Yu, J. A. Boscoboinik, S. Shaikhutdinov, and H. J. Freund, *J. Phys. Chem. C* **119**, 15443 (2015).
- [20] E. I. Altman, J. Götzen, N. Samudrala, and U. D. Schwarz, *J. Phys. Chem. C* **117**, 26144 (2013).
- [21] J.-H. Jhang, C. Zhou, O. E. Dagdeviren, G. S. Hutchings, U. D. Schwarz, and E. I. Altman, *Phys. Chem. Chem. Phys.* **19**, 14001 (2017).
- [22] L. Li, H. Tissot, S. Shaikhutdinov, and H. J. Freund, *Chem. Mater.* **29**, 931 (2017).
- [23] L. Lichtenstein, M. Heyde, and H. J. Freund, *J. Phys. Chem. C* **116**, 20426 (2012).
- [24] S. Shaikhutdinov and H. J. Freund, “Ultrathin silica films on metals: The long and winding road to understanding the atomic structure,” (2013).
- [25] H. Tissot, L. Li, S. Shaikhutdinov, and H. J. Freund, *Phys. Chem. Chem. Phys.* **18**, 25027 (2016).
- [26] D. L. Bish, *Clays Clay Miner.* **41**, 738 (1993).
- [27] M. Mellini and P. F. Zanazzi, *Am. Mineral.* **72**, 943 (1987).
- [28] J. M. D. Coey, A. Moukarika, and O. Ballet, *J. Appl. Phys.* **53**, 8320 (1982).
- [29] P. Bayliss, *Mineral. Mag.* **44**, 153 (1981).
- [30] A. Manceau, D. Chateigner, and W. P. Gates, *Phys. Chem. Miner.* **25**, 347 (1998).
- [31] L. G. Dainyak, B. B. Zviagina, V. S. Rusakov, and V. A. Drits, *Eur. J. Mineral.* **18**, 753 (2006).
- [32] P. J. Malden and R. E. Meads, *Nature* **215**, 844 (1967).
- [33] G. L. Woodward, C. L. Peacock, A. Otero-Fariña, O. R. Thompson, A. P. Brown, and I. T. Burke, *Geochim. Cosmochim. Acta* **238**, 270 (2018).
- [34] H. Shirozu and S. W. Bailey, *Am. Mineral.* **50**, 868 (1965).
- [35] G. W. Brindley and H.-M. Wan, *Am. Mineral.* **60**, 863 (1975).
- [36] R. D. White, D. V. Bavykin, and F. C. Walsh, *J. Mater. Chem. A* **1**, 548 (2013).
- [37] O. Ballet and J. M. Coey, *J. Phys. Colloq.* **39**, 765 (1978).
- [38] E. I. Parkhomenko, “Piezoelectric and Pyroelectric Effects in Minerals,” in *Electrif. Phenom. Rocks* (Springer US, Boston, MA, 1971) pp. 35–83.
- [39] G. Kresse and J. Furthmüller, *Comput. Mater. Sci.* **6**, 15 (1996).
- [40] G. Kresse and J. Furthmüller, *Phys. Rev. B. Condens. Matter* **54**, 11169 (1996).
- [41] J. Perdew, K. Burke, and M. Ernzerhof, *Phys. Rev. Lett.* **77**, 3865 (1996).
- [42] S. Dudarev and G. Botton, *Phys. Rev. B - Condens. Matter Mater. Phys.* **57**, 1505 (1998).
- [43] A. Jain, G. Hautier, S. P. Ong, C. J. Moore, C. C. Fischer, K. A. Persson, and G. Ceder, *Phys. Rev. B* **84**, 045115 (2011).
- [44] A. Jain, S. P. Ong, G. Hautier, W. Chen, W. D. Richards, S. Dacek, S. Cholia, D. Gunter, D. Skinner, G. Ceder, and K. A. Persson, *APL Mater.* **1**, 11002 (2013).
- [45] J. E. Saal, S. Kirklin, M. Aykol, B. Meredig, and C. Wolverton, *Journal of Materials* **65**, 1501 (2013).
- [46] V. Stevanovi, S. Lany, X. Zhang, and A. Zunger, *Phys. Rev. B* **85**, 115104 (2012).
- [47] K. A. Persson, B. Walldwick, P. Lazic, and G. Ceder, *Phys. Rev. B* **85**, 235438 (2012).
- [48] L. Wang, T. Maxisch, and G. Ceder, *Chem. Mater.* **19**, 543 (2007).
- [49] O. Kubaschewski, O. Kubaschewski, C. B. Alcock, and P. J. Spencer, *Materials Thermochemistry*, International series on materials science and technology (Pergamon Press, 1993).
- [50] R. D. King-Smith and D. Vanderbilt, *Phys. Rev. B* **47**, 1651 (1993).
- [51] R. Resta and D. Vanderbilt, *Top. Appl. Phys.* **105**, 31 (2007).
- [52] J. Neugebauer and M. Scheffler, *Phys. Rev. B* **46**, 16067 (1992).

- [53] See Supplementary Information.
- [54] A. Narayan, A. Bhutani, S. Rubeck, J. N. Eckstein, D. P. Shoemaker, and L. K. Wagner, *Phys. Rev. B - Condens. Matter Mater. Phys.* **94**, 045105 (2016), [arXiv:1512.02214](#).
- [55] W. A. Dollase, F. Seifert, and H. S. C. O'Neill, *Phys. Chem. Miner.* **21**, 104 (1994).
- [56] K. Persson, "Materials data on cr2sio4 (sg:70) by materials project," (2014), an optional note.
- [57] S. V. Streltsov and D. I. Khomskii, *Phys. Rev. B - Condens. Matter Mater. Phys.* **77** (2008), 10.1103/PhysRevB.77.064405.
- [58] G. J. Redhammer, G. Roth, W. Treutmann, M. Hoelzel, W. Paulus, G. André, C. Pietzonka, and G. Amthauer, *J. Solid State Chem.* **182**, 2374 (2009).
- [59] M. Berciu and R. N. Bhatt, *Phys. Rev. Lett.* **87**, 107203 (2001), [arXiv:0011319 \[cond-mat\]](#).
- [60] H. Shi, H. Pan, Y.-W. Zhang, and B. I. Yakobson, *Phys. Rev. B* **88**, 205305 (2013).
- [61] R. Mishra, W. Zhou, S. J. Pennycook, S. T. Pantelides, and J. C. Idrobo, *Phys. Rev. B - Condens. Matter Mater. Phys.* **88**, 144409 (2013).
- [62] H. Sato, K. Ono, C. T. Johnston, and A. Yamagishi, *Am. Mineral.* **90**, 1824 (2005).
- [63] S. V. Gallego, J. Etxebarria, L. Elcoro, E. S. Tasci, and J. M. Perez-Mato, *Acta Crystallogr. Sect. A Found. Adv.* **75**, 438 (2019).
- [64] B. Reynard, N. Hilairret, E. Balan, and M. Lazzeri, *Geophys. Res. Lett.* **34**, L13307 (2007).
- [65] S. Liu and R. E. Cohen, *Phys. Rev. Lett.* **119**, 1 (2017), [arXiv:1708.07240](#).
- [66] J. Liu, S. Liu, J. Y. Yang, and L. Liu, *Phys. Rev. Lett.* **125**, 197601 (2020).
- [67] C. Cui, F. Xue, W. J. Hu, and L. J. Li, *npj 2D Mater. Appl.* **2** (2018), 10.1038/s41699-018-0063-5.
- [68] S. Baroni, P. Giannozzi, and A. Testa, *Phys. Rev. Lett.* **58**, 1861 (1987).
- [69] C. Sevik, D. Çakır, O. Gülseren, and F. M. Peeters, *J. Phys. Chem. C* **120**, 13948 (2016).
- [70] R. Hinchet, U. Khan, C. Falconi, and S. W. Kim, *Mater. Today* **21**, 611 (2018).
- [71] M. T. Ong and E. J. Reed, *ACS Nano* **6**, 1387 (2012).